Inorganic Chemistry

pubs.acs.org/IC

Featured Article

Zinc-Catalyzed Two-Electron Nickel(IV/II) Redox Couple for Multi-Electron Storage in Redox Flow Batteries

Md. Motiur R. Mazumder, Niharika Dalpati, P. Raj Pokkuluri, and Byron H. Farnum*

Cite This: *Inorg. Chem.* 2022, 61, 19039−19048

Read Online

ACCESS | Metrics & More | Article Recommendations | Supporting Information

ABSTRACT: Energy storage is a vital aspect for the successful implementation of renewable energy resources on a global scale. Herein, we investigated the redox cycle of nickel(II) bis-(diethyldithiocarbamate), $Ni^{II}(dtc)_2$, for potential use as a multielectron storage catholyte in nonaqueous redox flow batteries (RFBs). Previous studies have shown that the unique redox cycle of $Ni^{II}(dtc)_2$ offers $2e^-$ chemistry upon oxidation from $Ni^{II} \rightarrow Ni^{IV}$ but $1e^-$ chemistry upon reduction from $Ni^{IV} \rightarrow Ni^{III} \rightarrow Ni^{II}$. Electrochemical experiments presented here show that the addition of as little as 10 mol % $Zn^{II}(ClO_4)_2$ to the electrolyte consolidates the two $1e^-$ reduction peaks into a single $2e^-$ reduction where $[Ni^{IV}(dtc)_3]^+$ is reduced directly to $Ni^{II}(dtc)_2$. This catalytic enhancement is believed to be due to Zn^{II} removal of a dtc^- ligand from a $Ni^{III}(dtc)_3$ intermediate, resulting in more facile reduction to $Ni^{II}(dtc)_2$. The addition of Zn^{II} also improves the $2e^-$ oxidation, shifting the anodic peak negative and decreasing the $2e^-$ peak separation. H-cell cycling experiments showed that 97% Coulombic efficiency and 98% charge storage efficiency was maintained for 50 cycles over 25 h using 0.1 M $Zn^{II}(ClO_4)_2$ as the supporting electrolyte. If $Zn^{II}(ClO_4)_2$ was replaced with $TBAPF_6$ in the electrolyte, the Coulombic efficiency fell to 78%. The use of Zn^{II} to increase the reversibility of $2e^-$ transfer is a promising result that points to the ability to use nickel dithiocarbonates for multielectron storage in RFBs.

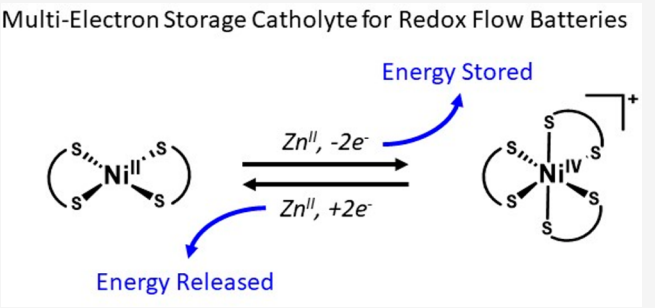

INTRODUCTION

The storage of electrical energy from renewable energy resources is paramount to their implementation on a large scale. Redox flow batteries (RFBs) address this important challenge through the use of small, molecular redox components in fluid solution.[1−5] These batteries are highly scalable and thus of direct interest for satisfying grid-scale energy storage. Given the molecular nature of RFBs, the energy stored is equal to the Gibbs free energy change for the combination of half-cell redox reactions, $\Delta G = -nF(E_c - E_a)$, where n is the number of stored electrons, E_c is the catholyte redox potential, and E_a is the anolyte redox potential. While strategies such as the use of nonaqueous solvents and tuning the E_c and E_a potentials have resulted in large battery voltages, increasing the number of electrons stored per molecule is an equally important strategy for increasing energy storage.[6−8]

Increasing the n-value beyond $1e^-$/molecule has been shown with both organic and inorganic molecules and clusters.[8−13] However, many of these examples have employed two sequential $1e^-$ redox couples to achieve multielectron storage. While this strategy indeed stores more electrons per molecule, each electron is not stored at the same potential and thus the charge−discharge voltage profile for the RFB displays a staircase pattern in which the voltage increases or decreases suddenly when moving between the two redox couples. An alternative strategy is to develop and employ molecules that operate with reversible $2e^-$ redox couples. This strategy has been used with anthraquinones for aqueous RFBs where proton-coupled electron transfer (PCET) generates potential inversion of the $1e^-$ redox potentials for the quinone/semiquinone and semiquinone/hydroquinone couples.[12] The result is reversible electrochemistry for the $2e^-$ quinone/hydroquinone redox couple.

Achieving reversible $2e^-$ chemistry with transition metal complexes is more challenging. Reversible, two-electron transfer reactions are uncommon for monometallic transition metal complexes and even more rare for first-row metals. Almost exclusively, the known examples of this reactivity utilize metal centers that convert between d^6 and d^8 electronic configurations while exploiting changes in ligand coordination to drive $2e^-$ transfer.[14−17] For example, Connick reported that square-planar $[Pt^{II}(NCN)(tpy)]^+$, where NCN is 1,3-bis-(piperidin-1-ylmethyl)benzene and tpy is terpyridine, undergoes outer-sphere $2e^-$ oxidation to $[Pt^{IV}(NCN)(tpy)]^{3+}$

Received: September 2, 2022
Published: November 22, 2022

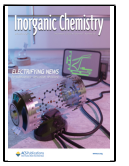

https://doi.org/10.1021/acs.inorgchem.2c03124
Inorg. Chem. 2022, 61, 19039−19048

coupled with coordination by the two piperidyl arms of the NCN ligand to form an octahedral complex.[16] Importantly, the redox couple also displays 2e⁻ reduction back to Pt^{II}, which is coincident with ligand dissociation. Ligand coordination to Pt^{IV} thus stabilizes the high valent metal center to generate potential inversion ($E°(Pt^{IV/III}) < E°(Pt^{III/II})$), making Pt^{III} unstable with respect to disproportionation. This ligand-coupled electron transfer (LCET) strategy is therefore central to the observation of reversible 2e⁻ transfer chemistry in monometallic transition metal complexes.

LCET is analogous to PCET in that chemical bond formation is associated with electron transfer. Whereas PCET uses H^+ to stabilize highly reduced species, LCET uses ligands, and thereby their donated electron density, to stabilize highly oxidized metal centers. Figure 1 shows a

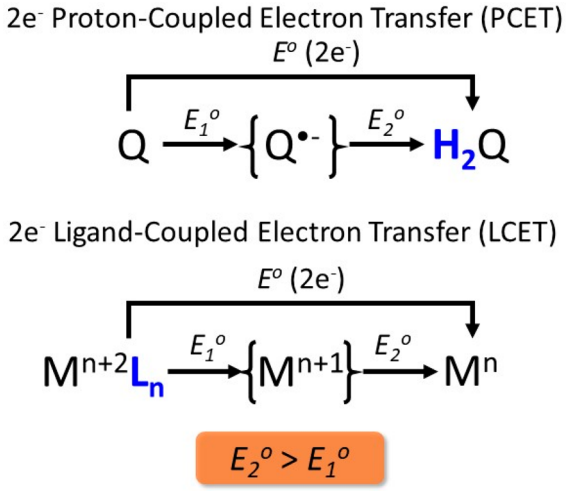

Figure 1. Comparison of Latimer diagrams for two-electron transfer reactions in which PCET and LCET drive potential inversion of the one-electron reduction potentials, $E_1°$ and $E_2°$. Q represents quinone and M represents a monometallic transition metal complex with ancillary ligands omitted for clarity.

comparison of Latimer diagrams for PCET and LCET from which two-electron transfer reactions may emerge. In both cases, the reduction potential for the second electron transfer ($E_2°$) is more favorable than the first electron transfer ($E_1°$). This results in an unstable intermediate, shown in brackets, and an overall two-electron transfer reaction. In both cases, structural distortions and changes in solvation free energies play large roles in forcing potential inversion.[18,19] PCET may operate by either stepwise or concerted mechanisms given that proton transfer is often a rapid process. In the case of LCET, ligand transfer rates are much slower than electron transfer and stepwise mechanisms prevail. These can be broken down into a combination of electron transfer and chemical steps. A common mechanism is the ECE pathway where electron transfer occurs first, followed by a chemical step such as ligand coordination, and finishes with the second electron transfer step.[18,20]

Rapid kinetics associated with the chemical step is paramount to the observation of reversible 2e⁻ transfer. In the Connick example and others in the literature, this is achieved through intramolecular ligand coordination with minimal reorganization of the ligand framework. In the present study, we show that rapid kinetics can also be achieved with intermolecular ligand transfer to achieve quasi-reversible 2e⁻ transfer chemistry despite large structural changes to the molecular framework. Specifically, we study the 2e⁻ LCET redox couple of $[Ni^{IV}(dtc)_3]^+/Ni^{II}(dtc)_2$, where dtc⁻ is N,N-diethyldithiocarbamate, in MeCN (eq 1). Chemical structures for $Ni^{II}(dtc)_2$ and $[Ni^{IV}(dtc)_3]^+$ are shown in Figure 2.

$$3/2Ni^{II}(dtc)_2 \rightleftharpoons [Ni^{IV}(dtc)_3]^+ + 1/2Ni^{II} + 2e^- \quad (1)$$

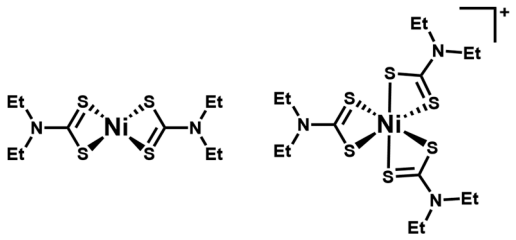

Figure 2. Chemical structures of $Ni^{II}(dtc)_2$ and $[Ni^{IV}(dtc)_3]^+$ where dtc⁻ is N,N-diethyldithiocarbamate.

Figure 3 shows a thermochemical cycle, or square scheme, to describe the electron transfer (horizontal) and ligand transfer

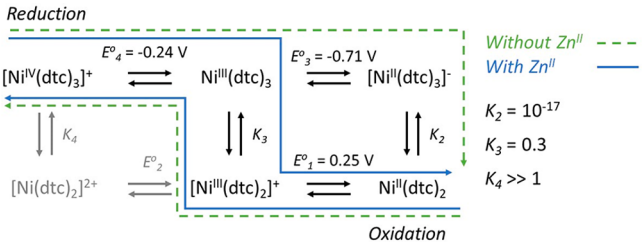

Figure 3. Thermochemical cycle describing the two-electron LCET $[Ni^{IV}(dtc)_3]^+/Ni^{II}(dtc)_2$ redox couple. One-electron transfer reactions are shown in the horizontal direction with potentials reported versus $Fc^{+/0}$ in MeCN with 0.1 M $TBAPF_6$. Ligand transfer reactions are shown in the vertical direction and represent the general reaction: (K_n) $[Ni^n(dtc)_2]^{2-n} + 1/2Ni^{II}(dtc)_2 \rightleftharpoons [Ni^n(dtc)_3]^{3-n} + 1/2Ni^{II}$. The green dashed lines indicate the sequence of reactions for oxidation and reduction without the presence of Zn^{II} ions. The blue solid lines indicate reactions in the same electrolyte with added Zn^{II} ions. The species $[Ni(dtc)_2]^{2+}$ and accompanying reactions are shown in gray to indicate that this species is hypothetical, and its inclusion is only meant to complete the thermochemical cycle.

(vertical) reactions for the $[Ni^{IV}(dtc)_3]^+/Ni^{II}(dtc)_2$ redox couple. The oxidation reaction, first reported in the 1970's,[21,22] proceeds through an RSD/ECE mechanism described by eqs 2−5 and the green dashed line shown in Figure 3.[23,24] RSD refers to radical substrate dimerization, a term derived from 2e⁻ electrochemistry with organic molecules,[18,25,26] which indicates that the chemical step involves reaction with a second equivalent of the substrate molecule (i.e., $Ni^{II}(dtc)_2$). Following oxidation of $Ni^{II}(dtc)_2$ to $[Ni^{III}(dtc)_2]^+$ (eq 2), the chemical step involves ligand transfer from $Ni^{II}(dtc)_2$ to $[Ni^{III}(dtc)_2]^+$ (eq 3) to produce the tris-chelated $Ni^{III}(dtc)_3$, whereby it can be oxidized a second time (eq 4) or disproportionate (eq 5) to result in $[Ni^{IV}(dtc)_3]^+$. It should be noted that $[Ni^{III}(dtc)_2]^+$ is expected to be solvent-coordinated (omitted here for clarity) based on experimental studies and theoretical calculations which suggest a five-coordinate $[Ni^{III}(dtc)_2(MeCN)]^+$ complex.[23,24] On the basis

https://doi.org/10.1021/acs.inorgchem.2c03124
Inorg. Chem. 2022, 61, 19039−19048

of the thermodynamic values for eqs 2−5, a reduction potential for eq 1 can be calculated to be $E^{\circ}(2e^{-}) = 0.02$ V vs $Fc^{+/0}$.

$$Ni^{II}(dtc)_2 \rightleftharpoons [Ni^{III}(dtc)_2]^+ + e^- \quad E_1^{\circ} = 0.25\ V\ (E) \tag{2}$$

$$[Ni^{III}(dtc)_2]^+ + 1/2Ni^{II}(dtc)_2 \rightleftharpoons Ni^{III}(dtc)_3 + 1/2Ni^{II} \quad K_3 = 0.28\ (C) \tag{3}$$

$$Ni^{III}(dtc)_3 \rightleftharpoons [Ni^{IV}(dtc)_3]^+ + e^- \quad E_4^{\circ} = -0.24\ V\ (E) \tag{4}$$

$$[Ni^{III}(dtc)_2]^+ + Ni^{III}(dtc)_3 \rightleftharpoons Ni^{II}(dtc)_2 + [Ni^{IV}(dtc)_3]^+ \quad K_{disp} = 2x10^8\ (DISP) \tag{5}$$

Despite $2e^-$ transfer being observed in the oxidation direction, sequential $1e^-$ transfer reactions are observed for reduction of $[Ni^{IV}(dtc)_3]^+$ back to $Ni^{II}(dtc)_2$ in MeCN (green dashed line in Figure 3) due to the mild stability of $Ni^{III}(dtc)_3$. The ligand transfer reaction shown in eq 3 is therefore critical to $2e^-$ chemistry as it allows rapid formation of $Ni^{III}(dtc)_3$ in the oxidation direction. Previous work has shown that strongly coordinating ligands such as pyridine can slow this reaction considerably by coordinating to the $[Ni^{III}(dtc)_2]^+$ intermediate, resulting in only $1e^-$ oxidation during cyclic voltammetry (CV) experiments.[23,24] The fact that $2e^-$ reduction of $[Ni^{IV}(dtc)_3]^+$ is not observed in MeCN suggests that the reverse reaction in eq 3 is kinetically slow. Therefore, efficient $2e^-$ reduction requires rapid conversion from $Ni^{III}(dtc)_3$ to $[Ni^{III}(dtc)_2]^+$.

Electrochemical modeling of CV data for $Ni^{II}(dtc)_2$ in MeCN with 0.1 M $TBAPF_6$ have calculated the equilibrium constant for eq 3 to be $K_3 = 0.28$.[24] This means the conversion from $[Ni^{III}(dtc)_2]^+$ to $Ni^{III}(dtc)_3$ is slightly disfavored. However, CV data clearly show favorable $2e^-$ oxidation and unfavorable $2e^-$ reduction. We believe this is due to the fact that during oxidation, excess $Ni^{II}(dtc)_2$ is available in the electrolyte solution which drives the reaction toward production of $Ni^{III}(dtc)_3$. In contrast, the reverse direction requires Ni^{II} ions which are only generated in low concentration during oxidation, thus limiting the production of $[Ni^{III}(dtc)_2]^+$ and therefore $2e^-$ reduction. Thus, if excess Ni^{II} ions were added to the electrolyte solution, the kinetics for the formation of $[Ni^{III}(dtc)_2]^+$ could be improved. Once $[Ni^{III}(dtc)_2]^+$ is formed, $1e^-$ reduction or disproportionation with $Ni^{III}(dtc)_3$ are both thermodynamically favored pathways to ultimately yield the starting $Ni^{II}(dtc)_2$ species.

In the present study, we show that the addition of $Ni^{II}(ClO_4)_2$ or $Zn^{II}(ClO_4)_2$ to the electrolyte solution results in efficient $2e^-$ reduction from $[Ni^{IV}(dtc)_3]^+$ to $Ni^{II}(dtc)_2$ (solid blue line in Figure 3). These ions are shown to drive the conversion of $Ni^{III}(dtc)_3$ to $[Ni^{III}(dtc)_2]^+$ through removal of a dtc^- ligand according to the reverse reaction of eq 2. Most importantly, Zn^{II} ions are further shown to act as catalysts for this reaction due to the quantitative conversion of $Zn^{II}(dtc)_2$ to $Ni^{II}(dtc)_2$ in the presence of Ni^{II} ions. We further show that this Zn^{II}-catalyzed $2e^-$ $Ni^{IV/II}$ redox couple can be cycled electrochemically in an H-cell to mimic an RFB for 25 h with 97% Coulombic efficiency and 98% charge storage retention. In contrast, the absence of $Zn^{II}(ClO_4)_2$ results in rapid degradation of the Coulombic efficiency due to incomplete reduction back to $Ni^{II}(dtc)_2$. Implications of this $2e^-$ redox cycle on the discovery of new, inorganic catholytes for RFBs is highlighted.

EXPERIMENTAL SECTION

General Considerations. All chemicals were used as received unless otherwise indicated. ^{1}H NMR experiments were performed with a Bruker 500 MHz instrument. UV−visible absorbance spectroscopy was performed with an Agilent Technologies Cary 8454 photodiode array spectrophotometer. Single crystal X-ray crystallography was performed on a Bruker D8 VENTURE κ-geometry diffractometer using either Mo Kα (λ = 0.71073 Å) or Cu Kα (λ = 1.54178 Å) radiation (Incoatec IμS DIAMOND microfocus sealed tube and a multilayer mirror monochromator). The integrations and global cell refinements were performed by using APEX3 software which includes the Bruker SAINT software package. Structures were solved by using Intrinsic Phasing/Direct Methods (ShelXT),[27] and least-squares refinement was performed using ShelXL in APEX3. Mass spectrometry analyses were performed on a quadrupole orbitrap mass spectrometer (Explorus 120, Thermo Fisher) with electrospray ionization (ESI) in positive mode using Xcalibur software.

Synthesis and Characterization. $Ni^{II}(dtc)_2$ was synthesized by adding two equivalents of sodium diethyldithiocarbamate trihydrate ($Na(dtc)\cdot 3H_2O$, Sigma-Aldrich, >99%) to one equivalent of nickel(II) chloride hexahydrate (Alfa Aesar, 98%) in DI water as described previously.[22−24] A light-green solid precipitated instantly and was filtered under vacuum and washed with cold distilled water, ethanol, and ether to obtain 96% yield. Characterization of the light-green solid was performed by ^{1}H NMR (acetonitrile-d_3, CD_3CN, Cambridge Isotopes): δ 3.60 (q, $-CH_2-$), 1.21 (t, $-CH_3$), UV−visible absorbance spectroscopy: λ_{max} (ε) = 388 nm (5,600 M^{-1} cm^{-1}) and 323 nm (26,700 M^{-1} cm^{-1}), and X-ray crystallography. X-ray quality crystals were grown by slow evaporation in dichloromethane (DCM, Sigma-Aldrich, ≥99.5%). X-ray crystal data matched that of a previous publication.[28]

$Zn^{II}(dtc)_2$ was synthesized by the same method described for $Ni^{II}(dtc)_2$, expect with zinc acetate dihydrate (Alfa Aesar, 97%) as the Zn^{II} source. A white solid was obtained in 96% yield and characterized by ^{1}H NMR (CD_3CN): δ 3.90 (q, $-CH_2-$), 1.32 (t, $-CH_3$) and X-ray crystallography. X-ray quality crystals were grown by slow evaporation in DCM. X-ray crystal data is shown in Figure S1.

$[Ni^{IV}(dtc)_3]BF_4$ was synthesized by oxidizing $Ni^{II}(dtc)_2$ following a modified literature procedure using ∼1.3 equiv of $NOBF_4$ (BTC, 98%) in DCM instead of boron trifluoride etherate as the oxidant.[22] Upon addition of $NOBF_4$, the solution turned dark brown and was kept stirring for 3 h. Filtration followed by solvent evaporation of the filtrate produced the desired reddish-brown solid in 80% yield. Characterization was performed by ^{1}H NMR (CD_3CN): δ 3.68 (q, $-CH_2-$) and 1.28 (t, $-CH_3$), ESI-MS: (*m*/*z*) for $[C_{15}H_{30}N_3S_6Ni]^+$: 502.0117 (calc), 502.0112 (found), UV−visible absorbance spectroscopy: λ_{max} (ε) = 437 nm (9,800 M^{-1} cm^{-1}) and 495 nm (7,500 M^{-1} cm^{-1}), and X-ray crystallography. Crystals of $[Ni^{IV}(dtc)_3]BF_4$ were grown by solvent diffusion of diethyl ether into an acetonitrile solution containing the dissolved solid. X-ray crystal data is shown in Figure S2.

Electrochemistry. All experiments were performed in acetonitrile solvent (MeCN, HPLC grade, VWR Chemicals) using 0.1 M $TBAPF_6$, $Zn^{II}(ClO_4)_2\cdot 6H_2O$ (Sigma-Aldrich, 98%), $Ni^{II}(ClO_4)_2\cdot 6H_2O$ (Sigma-Aldrich, 98%), $Mg^{II}(ClO_4)_2\cdot 6H_2O$ (Sigma-Aldrich, 99%), $Ca^{II}(ClO_4)_2\cdot 6H_2O$ (Sigma-Aldrich, 99%), or $Zn^{II}(BF_4)_2\cdot xH_2O$ (Sigma-Aldrich) as supporting electrolytes in a nitrogen-purged environment at room temperature. **Caution!** Metal complexes containing perchlorate ions are potentially explosive and should be handled with care. Tetrabutylammonium hexafluorophosphate ($TBAPF_6$; Sigma-Aldrich, 98%) was recrystallized twice in absolute ethanol, then dehydrated under vacuum, and kept in a desiccator until further use. $Zn^{II}(ClO_4)_2$ and $Ni^{II}(ClO_4)_2$ were used as received. Cyclic voltammetry (CV), square wave voltammetry (SWV), and rotating disk electrochemistry (RDE) were performed with a WaveDriver 20 bipotentiostat (Pine Research) using a rotating ring-disk working electrode (E6 change disk, Pine Research) containing a 5 mm diameter glassy-carbon disk and platinum ring, a Ag wire

https://doi.org/10.1021/acs.inorgchem.2c03124
Inorg. Chem. 2022, 61, 19039−19048

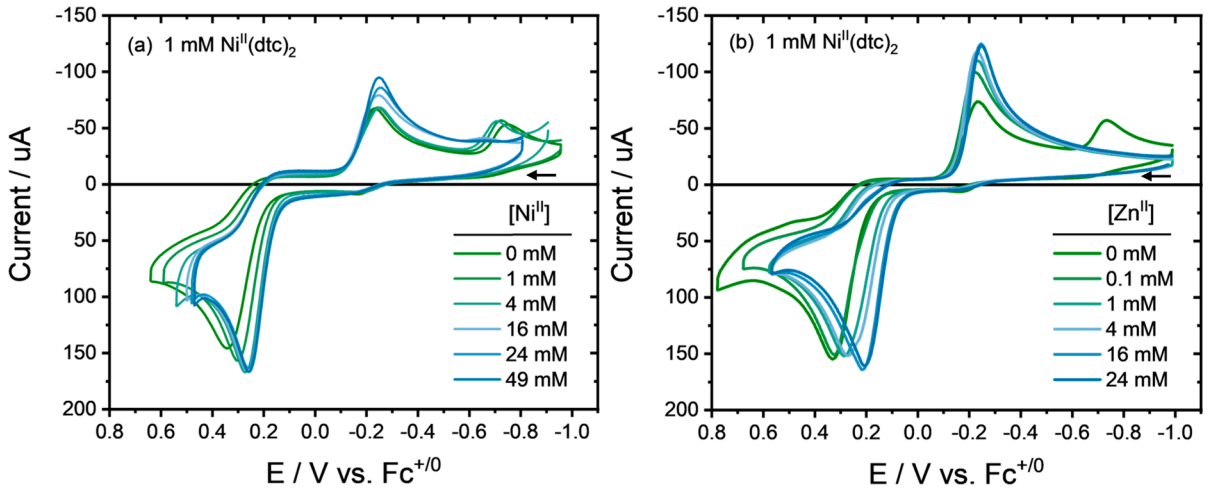

Figure 4. CV data collected for 1 mM $Ni^{II}(dtc)_2$ in MeCN with 0.1 M $TBAPF_6$ as a function of added (a) $Ni^{II}(ClO_4)_2$ and (b) $Zn^{II}(ClO_4)_2$. Legends indicate $[Ni^{II}]$ and $[Zn^{II}]$. The scan rate for each plot is 631 mV/s. The arrow indicates the initial scanning direction.

nonaqueous reference electrode in MeCN (0.1 M $TBAPF_6$) housed in a fritted glass tube (BASi), and a platinum wire counter electrode. An alumina suspension (0.05 μm alumina powder, Allied High-tech Products Inc., DeAgglomerated) was used to polish the working electrode before every experiment. Ferrocene (Fc; Alfa Aesar, 99%) was used as an external reference for the applied potential wherein the redox potential of Fc was recorded before and after all electrochemical experiments using the same reference electrode in the same electrolyte. All potentials are thus reported versus the $Fc^{+/0}$ couple. The internal solution resistance was compensated in all experiments and was generally found to be ~120 Ω.

CV experiments with $Ni^{II}(dtc)_2$ were performed as a function of scan rate and consisted of three continuous cycles starting at the negative extreme potential and scanning in a positive direction. CV experiments with $[Ni^{IV}(dtc)_3]BF_4$ were performed in a similar way by starting at the positive extreme potential and scanning in a negative direction. Presented CV data represents the third cycle. Addition of $Zn^{II}(ClO_4)_2$ or $Ni^{II}(ClO_4)_2$ during CV experiments was achieved by dissolving the salts in MeCN and purging with nitrogen before titration into the electrolyte solution. SWV experiments were performed with a 20 mV amplitude, 0.1 s period, 2 mV increment, and 1 ms sample width. RDE experiments were performed at a constant scan rate of 50 mV s^{-1} and variable rotation rate.

H-Cell Battery Experiments. Chronopotentiometric battery experiments were performed in an electrochemical H-cell with catholyte and anolyte chambers divided by an AMI-7000s anion-exchange membrane (Membranes International Inc.) under a nitrogen-purged atmosphere. The catholyte chamber contained 1 mM $Ni^{II}(dtc)_2$ in MeCN with either 0.1 M $TBAPF_6$ plus a titrated concentration of $Zn^{II}(ClO_4)_2$ or 0.1 M $Zn^{II}(ClO_4)_2$. The anolyte solutions consisted of either 0.1 M $TBAPF_6$ in MeCN for Zn^{II} titration experiments or 0.1 M $TBAPF_6$ and 0.2 M $[MV](PF_6)_2$ in MeCN for extended cycling experiments. Here, $[MV]^{2+}$ is methyl viologen where $[MV](PF_6)_2$ was metathesized from $[MV]Cl_2$ (Sigma-Aldrich, 98%) by dissolving in water and adding KPF_6 (Sigma-Aldrich, ≥ 99%) to precipitate the desired product.

Experiments were performed with a CH Instruments 600E potentiostat in a three-electrode configuration with two graphite-felt electrodes (Fuel cell store, geometric surface area 8 cm^2) used as working and counter electrodes and a Ag wire nonaqueous reference electrode in MeCN (0.1 M $TBAPF_6$) housed in a fritted glass tube. The entire H-cell apparatus was wrapped in foil to prevent light penetration to the cell as $[Ni^{IV}(dtc)_3]BF_4$ undergoes photo-decomposition in MeCN. The volume of each catholyte and anolyte solution was 9.7 mL, and each chamber was magnetically stirred at 800 rpm. The anion-exchange membrane was presoaked in a solution containing MeCN and 0.1 M $TBAPF_6$ for 24 h prior to each experiment. Chronopotentiometric charge (anodic at the working electrode) and discharge (cathodic at the working electrode) currents were 2 mA and 1 mA, respectively. Charge cycles were run up to 0.48 V vs $Fc^{+/0}$ and discharge cycles down to −0.92 V vs $Fc^{+/0}$.

RESULTS AND DISCUSSION

Two-Electron Reduction Enhanced by M^{II} Cations. Cyclic voltammetry was performed with 1 mM $Ni^{II}(dtc)_2$ in MeCN solvent with a 0.1 M $TBAPF_6$ electrolyte as a function of added $Ni^{II}(ClO_4)_2$ or $Zn^{II}(ClO_4)_2$. Figure 4a shows the effect of Ni^{II} ions on the $Ni^{II}(dtc)_2$ redox chemistry. The second reduction wave near −0.7 V ($Ni^{III}(dtc)_3/[Ni^{II}(dtc)_3]^-$) decreased and shifted in a positive direction for added Ni^{II} with respect to the initial condition. Concomitant with these changes was the noticeable increase in current at the first reduction wave near −0.3 V ($[Ni^{IV}(dtc)_3]^+/Ni^{III}(dtc)_3$). On the basis of eq 3, the addition of Ni^{II} ions should drive the reaction toward production of $[Ni^{III}(dtc)_2]^+$ following the first reduction, thus allowing for reduction by a second electron or disproportionation via eq 5. Note that with an applied potential of −0.3 V vs $Fc^{+/0}$, the driving force for reduction of $[Ni^{III}(dtc)_2]^+$ to $Ni^{II}(dtc)_2$ is −0.55 eV, and the free energy change for disproportionation is ΔG°_{DISP} = −0.49 eV. The addition of Ni^{II} gives a proof of principle for enhancing $2e^-$ reduction; however, a large concentration of $Ni^{II}(ClO_4)_2$ was required to increase the cathodic current substantially. Therefore, other M^{II} redox inert cations were explored as ligand acceptors which could promote $2e^-$ reduction.

Among the M^{II} redox inert cations studied (Zn^{II}, Ca^{II}, and Mg^{II}), the addition of $Zn^{II}(ClO_4)_2$ was also found to greatly enhance the $2e^-$ reduction of $[Ni^{IV}(dtc)_3]^+$ to $Ni^{II}(dtc)_2$. Figure 4b shows CV data for $Zn^{II}(ClO_4)_2$ addition where changes were similar as with Ni^{II}; however, the current increase at the first reduction peak occurred at lower $[Zn^{II}]$ than was observed for $[Ni^{II}]$. We believe the ability of both Zn^{II} and Ni^{II} to act as suitable dtc^- ligand acceptors lies in the fact that both are intermediate Lewis acids and have favorable coordination with the soft base sulfur atoms of the dtc^- ligand. The greater $2e^-$ enhancement in the case of Zn^{II} points to faster kinetics for dtc^- ligand removal for Zn^{II} versus Ni^{II}. This could be due to a slightly higher charge density and/or more labile coordination sphere of Zn^{II}. Each ion is likely coordinated by solvent molecules prior to dtc^- ligand removal, thus a greater lability of the Zn^{II} ion may promote fast removal of MeCN ligands and

https://doi.org/10.1021/acs.inorgchem.2c03124
Inorg. Chem. 2022, 61, 19039−19048

facilitate the coordination of dtc^-. Control experiments for the addition of H_2O and the use of $Zn^{II}(BF_4)_2$ as electrolyte indicated that H_2O and ClO_4^- do not play a significant role in $2e^-$ enhancement (Figure S4). The addition of H_2O had no impact on the overall redox cycle and the use of $Zn^{II}(BF_4)_2$ resulted in the same $2e^-$ reduction observed for $Zn^{II}(ClO_4)_2$. Furthermore, CV data collected in the presence of Mg^{II} and Ca^{II} are shown in Figures S5 and S6, where the enhancement in $2e^-$ reduction was also noted but the magnitude of increased current near −0.3 V was minimal compared with Ni^{II} and Zn^{II}, even at high concentrations of the M^{II} cations. We believe the diminished impact of these hard Lewis acids further supports the soft acid−base hypothesis for Ni^{II} and Zn^{II}.

Although we believe that Zn^{II} aids in the removal of dtc^- ligands, it is important to note that $Zn^{II}(dtc)_2$ products were not found to build up in the solution through repeated cycling of the applied potential in the CV experiment. Thus, Zn^{II} ions act purely as catalysts to remove the dtc^- ligand and must then deliver this ligand to a Ni^{II} ion (generated during oxidation to $[Ni^{IV}(dtc)_3]^+$) in order to regenerate $Ni^{II}(dtc)_2$. UV−visible absorbance spectroscopy data confirmed that the reaction between $Zn^{II}(dtc)_2$ and Ni^{II} ions strongly favors the exchange of dtc^- ligands to generate $Ni^{II}(dtc)_2$ and Zn^{II} (Figure S7). These studies show that addition of $Ni^{II}(ClO_4)_2$ to a solution of $Zn^{II}(dtc)_2$ in MeCN result in quantitative formation of $Ni^{II}(dtc)_2$ according to eq 6.

$$Zn^{II}(dtc)_2 + Ni^{II} \rightleftharpoons Zn^{II} + Ni^{II}(dtc)_2 \quad K_{eq} >> 1 \tag{6}$$

Electrochemical studies with $[Ni^{IV}(dtc)_3]^+$ as the starting material also showed an increase in current at the first reduction wave as Zn^{II} was introduced into solution. Figure 5

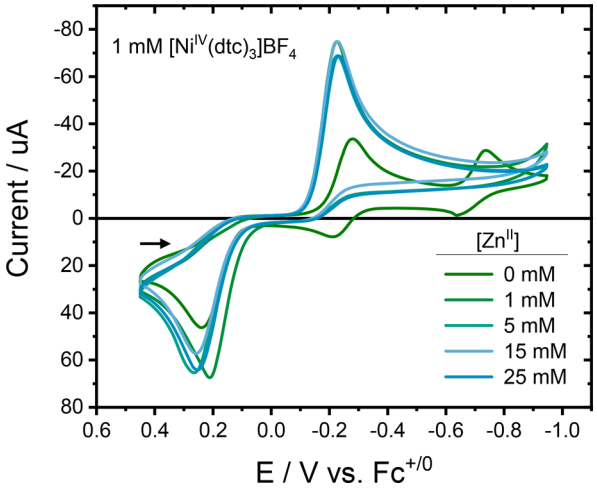

Figure 5. CV data collected for 1 mM $[Ni^{IV}(dtc)_3]^+$ in MeCN with 0.1 M $TBAPF_6$ as a function of added $Zn^{II}(ClO_4)_2$ at a scan rate of 100 mV/s. The arrow indicates the initial scanning direction.

shows CV data collected for 1 mM $[Ni^{IV}(dtc)_3]BF_4$ in MeCN with 0.1 M $TBAPF_6$ as a function of added $Zn^{II}(ClO_4)_2$. The initial CV in the absence of Zn^{II} showed higher reversibility at the $[Ni^{IV}(dtc)_3]^+/Ni^{III}(dtc)_3$ and $Ni^{III}(dtc)_3/[Ni^{II}(dtc)_3]^-$ redox waves than was observed for the $Ni^{II}(dtc)_2$ starting material due to the fact that no Ni^{II} cations were initially present in solution to accept the dtc^- ligand from $[Ni^{II}(dtc)_3]^-$. Therefore, the anodic scan showed measurable current for the oxidation of these redox couples. Nonetheless, decomposition of $[Ni^{II}(dtc)_3]^-$ to $Ni^{II}(dtc)_2$ must occur to some extent on the CV time scale due to the observed oxidation peak near 0.2 V.

Upon addition of $Zn^{II}(ClO_4)_2$, the CV changed to resemble that of Figure 4b by increasing the current at the $[Ni^{IV}(dtc)_3]^+/Ni^{III}(dtc)_3$ wave and decreasing the current at the $Ni^{III}(dtc)_3/[Ni^{II}(dtc)_3]^-$ wave. A notable increase in the anodic current for $Ni^{II}(dtc)_2$ oxidation was also observed due to the enhancement of $2e^-$ reduction from $[Ni^{IV}(dtc)_3]^+$ to $Ni^{II}(dtc)_2$ with Zn^{II} addition. Interestingly, the peak potential for $2e^-$ reduction in the presence of Zn^{II} showed a 50 mV shift in the positive direction from the initial peak in the absence of Zn^{II}. We believe this is the result of an ECE mechanism in which the chemical step involves Zn^{II} reacting with $Ni^{III}(dtc)_3$ to remove a dtc^- ligand and produce $[Ni^{III}(dtc)_2]^+$ (eq 7). EC and ECE mechanisms are known to shift the reduction peak in a positive direction due to consumption of the initial reduced product.[18] Scan rate dependent studies (Figure S8) also support this conclusion, indicating a consistent positive shift of the cathodic peak and increase in peak current with lower scan rates. This observation means the chemical step occurs on the CV time scale where lower scan rates allow for further consumption of the initially reduced product $Ni^{III}(dtc)_3$ (shifting the peak) and for further reduction to $Ni^{II}(dtc)_2$ (higher current). Eq 7 is essentially the reverse of eq 3 with Zn^{II} substituted for Ni^{II} and helps to explain the similarities observed between Ni^{II} and Zn^{II} additions with $Ni^{II}(dtc)_2$ solutions. Reduction of $[Ni^{III}(dtc)_2]^+$ (reversed eq 2) or disproportionation of $[Ni^{III}(dtc)_2]^+$ with $Ni^{III}(dtc)_3$ (eq 5) would result in overall $2e^-$ reduction to $Ni^{II}(dtc)_2$.

$$Ni^{III}(dtc)_3 + 1/2Zn^{II} \rightleftharpoons [Ni^{III}(dtc)_2]^+ + 1/2Zn^{II}(dtc)_2 \tag{7}$$

Two-Electron Oxidation Enhanced by M^{II} Cations. Surprisingly, the addition of Ni^{II} and Zn^{II} also improved $2e^-$ oxidation of $Ni^{II}(dtc)_2$, which shifted the anodic peak slightly negative and thus decreased the overall peak separation between anodic and cathodic peaks (Figure 4b). Square wave voltammetry performed as a function of $[Zn^{II}]$ for $Ni^{II}(dtc)_2$ solutions revealed that the original anodic peak at E_{p1} = 0.25 V decreased in magnitude and shifted in the negative direction as a function of $[Zn^{II}]$ while a new peak at E_{p2} = 0.15 V increased in current with no observable shift (Figure 6). E_{p1} is consistent with the redox potential for $[Ni^{III}(dtc)_2]^+/Ni^{II}(dtc)_2$ which starts the $2e^-$ oxidation process. The negative shift in the peak suggests that a rapid follow up reaction with Zn^{II} is present, which consumes $[Ni^{III}(dtc)_2]^+$ along the path to formation of $[Ni^{IV}(dtc)_3]^+$ via an ECE mechanism. However, the growth of E_{p2} with $[Zn^{II}]$ indicates the formation of a new species prior to oxidation and implies an equilibrium between $Ni^{II}(dtc)_2$ and Zn^{II} to form an encounter complex (eq 8).

$$Ni^{II}(dtc)_2 + Zn^{II} \rightleftharpoons \{Ni^{II}(dtc)_2—Zn^{II}\} \quad K_{eq} = 147\ M^{-1} \tag{8}$$

$$[Ni^{II}(dtc)_2—Zn^{II}] = (K_{eq}[Zn^{II}])/(1 + K_{eq}[Zn^{II}]/b) \tag{9}$$

^1H NMR studies also supported the formation of a new species through monitoring the methyl and methylene peaks of the dithiocarbamate ligands (Figure 7a and Figure S9). Both sets of protons show distinctly new peaks with the addition of $Zn^{II}(ClO_4)_2$ to a 1 mM solution of $Ni^{II}(dtc)_2$ in CD_3CN. These new peaks are different from those found for $Zn^{II}(dtc)_2$;

https://doi.org/10.1021/acs.inorgchem.2c03124
Inorg. Chem. 2022, 61, 19039−19048

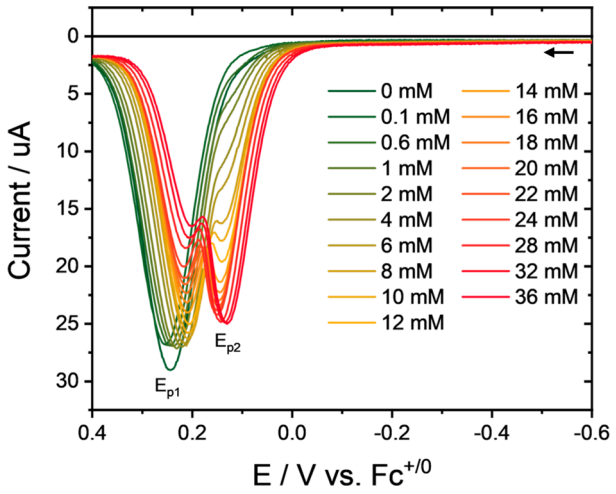

Figure 6. Square wave voltammetry data collected for 1 mM $Ni^{II}(dtc)_2$ in MeCN with 0.1 M $TBAPF_6$ as a function of added $[Zn^{II}]$. The arrow indicates the scanning direction.

therefore, equilibration to form $Zn^{II}(dtc)_2$ (eq 6) can be ruled out, in agreement with UV−visible absorbance studies discussed above. Figure 7b shows a plot of the normalized peak areas for the methyl protons associated with free $Ni^{II}(dtc)_2$ and those of the encounter complex, termed $\{Ni^{II}(dtc)_2\text{-}Zn^{II}\}$. Clearly, as the complex is formed, the area for $Ni^{II}(dtc)_2$ decreases; however, both data sets asymptotically approach a normalized area near 0.5 at high $[Zn^{II}]$. Given that the $Ni^{II}(dtc)_2$ complex is a square planar geometry with dithiocarbamate ligands oriented on opposite sides of the molecule, this result indicates that Zn^{II} is only able to interact with one of the two dithiocarbamate ligands. Fitting the growth of $\{Ni^{II}(dtc)_2\text{-}Zn^{II}\}$ to eq 9 allowed for an equilibrium constant for eq 8 of 147 M^{-1} to be extracted. In this equation, the b parameter is used to indicate the fraction of dtc^- ligands that Zn^{II} influences. The best fit value was b = 0.43, close to the expected value of 0.5 for a 50% interaction.

The exact nature of the Zn^{II} interaction with dtc^- ligands is unknown; however, the X-ray crystal structure of $Zn^{II}(dtc)_2$ (Figure S1) shows a dimer structure with a slip-stacked orientation where Zn^{II} ions are positioned above the sulfur atoms of adjacent molecules to form a square-based pyramidal geometry. We thus propose that association of Zn^{II} occurs through coordination with the sulfur atoms of $Ni^{II}(dtc)_2$. Interestingly, the difference of E_{p1} and E_{p2} values shows that association of Zn^{II} ions with the initial oxidized product, $[Ni^{III}(dtc)_2]^+$, is more favorable than $Ni^{II}(dtc)_2$ by a factor of 50 (Supporting Information). This result is surprising given the cationic charges of Zn^{II} and $[Ni^{III}(dtc)_2]^+$ and may suggest that the charge of Zn^{II} is neutralized by closely associated PF_6^- and/or ClO_4^- anions.

Two-Electron Reversibility Measurements. Given that the addition of Ni^{II} and Zn^{II} increased $2e^-$ reduction, the replacement of $TBAPF_6$ with $Ni^{II}(ClO_4)_2$ or $Zn^{II}(ClO_4)_2$ as the supporting electrolyte was explored. Notably, both salts have lower molecular weights than $TBAPF_6$, and thus, replacement also provides a benefit to mass density for RFB applications. Diffusion coefficients for $Ni^{II}(dtc)_2$ and $[Ni^{IV}(dtc)_3]^+$ were also similar as a function of electrolyte conditions (Table S3). Figure 8 shows CV data collected for 1 mM $Ni^{II}(dtc)_2$ in either 0.1 M $Ni^{II}(ClO_4)_2$ and 0.1 M $Zn^{II}(ClO_4)_2$ normalized as a function of scan rate ($iv^{-1/2}$). A plot of $-i_{pc}/i_{pa}$ versus $\log(v)$ for each electrolyte is shown in Figure 9. The ratio of $-i_{pc}/i_{pa}$ was taken as the raw current with no corrections for nonfaradaic current. While both cases are clearly better than $TBAPF_6$, one can see that $Zn^{II}(ClO_4)_2$ displays the highest reversibility over the widest range in scan rates with a maximum of $-i_{pc}/i_{pa}$ = 0.81 at 251 mV/s. The decrease in $-i_{pc}/i_{pa}$ for $Ni^{II}(ClO_4)_2$ from its maximum of 0.77 at 100 mV/s toward high scan rates can be attributed to the slower kinetics for dtc^- ligand removal with Ni^{II} versus Zn^{II}. As the scan rate was increased, dtc^- ligand removal from $Ni^{III}(dtc)_3$ could not keep up and the cathodic peak current decreased, as shown in Figure 8a.

Although a perfectly reversible redox couple should display a peak current ratio of 1, in practice the maximum peak current ratio for ferrocene (the $1e^-$ reversible standard) was found to be 0.86 due to diffusion of the oxidized species away from the electrode surface and the fact that no correction to the peak currents were made for the nonfaradaic current. Thus, a comparison with the maximum value of $-i_{pc}/i_{pa}$ = 0.81 found

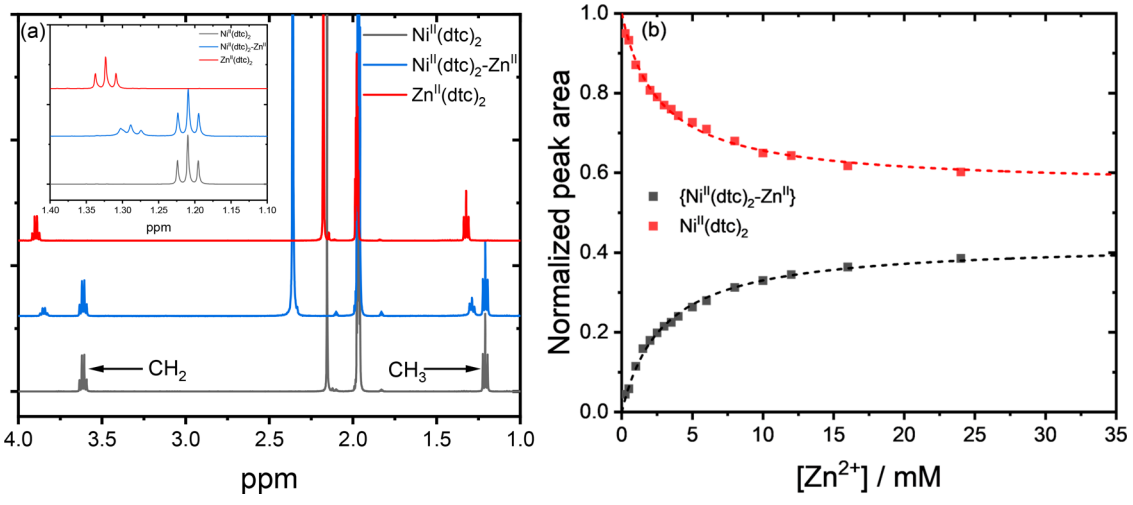

Figure 7. (a) ^1H NMR spectra collected in CD_3CN of 1 mM $Ni^{II}(dtc)_2$ (dark gray), 1 mM $Zn^{II}(dtc)_2$ (red), and 1 mM $Ni^{II}(dtc)_2$ with 10 mM $Zn^{II}(ClO_4)_2$ (blue). (b) Integrated peak intensities for methyl protons associated with free $Ni^{II}(dtc)_2$ (red) and bound $\{Ni^{II}(dtc)_2\text{-}Zn^{II}\}$ (dark gray). Dashed lines represent fits to eq 9 used to extract the equilibrium constant for $\{Ni^{II}(dtc)_2\text{-}Zn^{II}\}$ formation.

https://doi.org/10.1021/acs.inorgchem.2c03124
Inorg. Chem. 2022, 61, 19039−19048

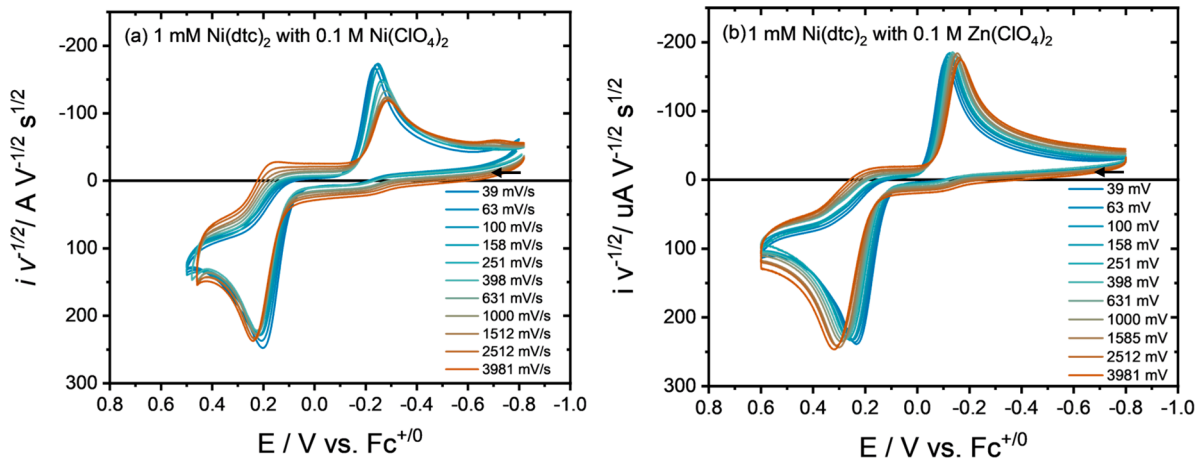

Figure 8. CV data collected for 1 mM $Ni^{II}(dtc)_2$ as a function of scan rate in MeCN with (a) 0.1 M $Ni^{II}(ClO_4)_2$ and (b) 0.1 M $Zn^{II}(ClO_4)_2$ supporting electrolytes. The arrow indicates the initial scanning direction.

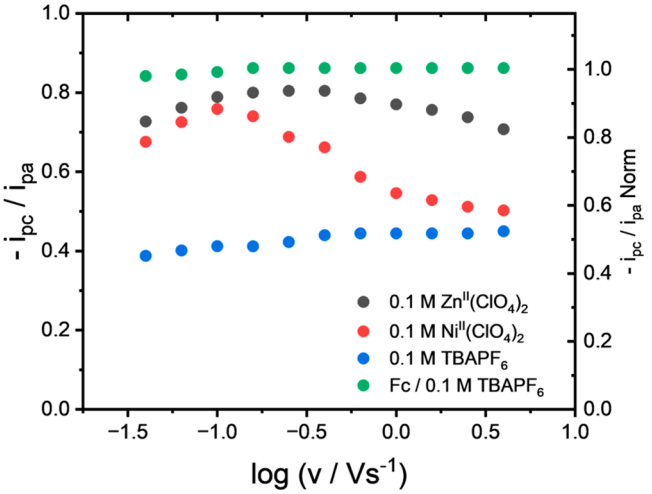

Figure 9. Comparison of $2e^-$ reversibility among supporting electrolytes based on a ratio of peak currents $-i_{pc}/i_{pa}$ as a function of scan rate for 1 mM $Ni^{II}(dtc)_2$. Ferrocene ($1e^-$ couple) standard data collected in MeCN with 0.1 M $TBAPF_6$ provided for comparison. Right axis shows $-i_{pc}/i_{pa}$ normalized to the maximum value obtained for ferrocene.

for the 0.1 M $Zn^{II}(ClO_4)_2$ electrolyte yields a $2e^-$ reversibility of 94% based on peak current.

Reversibility is also defined by the anodic and cathodic peak separation with an ideal value of 28 mV for a $2e^-$ redox couple. However, the peak separation measured for 1 mM $Ni^{II}(dtc)_2$ with 0.1 M $Zn^{II}(ClO_4)_2$ was 330 mV. This large peak separation is the result of the significant structural rearrangement which occurs between square planar $Ni^{II}(dtc)_2$ and pseudo-octahedral $[Ni^{IV}(dtc)_3]^+$. Despite the large peak separation, the individual $2e^-$ oxidation and reduction waves were found to be close to the electrochemically reversible limit defined by the peak-width $E_p - E_{p/2}$, where E_p is the peak potential and $E_{p/2}$ is the potential where half of the peak current is achieved. This metric can be used for linear sweep voltammograms where the return wave is not measured or for chemically irreversible redox reactions that display fast electron transfer kinetics in the forward direction. For an electrochemically reversible wave, $E_p - E_{p/2}$ = 57 mV/n, where n is the number of electrons transferred per reactant molecule. In the case of ferrocene, $E_p - E_{p/2}$ = 61 mV at a 39 mV/s scan rate, close to the ideal value for $1e^-$ transfer (Figure S10). This value increased as a function of scan rate up to 78 mV at 3981 mV/s. The drift in peak-width is thus an indication of electrochemical quasi-reversibility due to electron transfer kinetics, causing the peak to become broader at higher scan rates.

For 1 mM $Ni^{II}(dtc)_2$ in 0.1 M $Zn^{II}(ClO_4)_2$, $E_p - E_{p/2}$ was found to be 35 mV at 39 mV/s for the reduction reaction (Figure S10), close to the ideal 29 mV difference for n = 2, and only increased to 41 mV by 3981 mV/s, indicating fast electron transfer kinetics. The oxidation reaction was slightly higher at $E_p - E_{p/2}$ = 43 mV for 39 mV/s and increased to 65 mV at 3981 mV/s. Notably, the n-value for the oxidation reaction is actually n = 4/3 based on the stoichiometry of eq 1 (i.e., $2e^-$ transferred for every 3/2 $Ni^{II}(dtc)_2$) and thus an expected value of $E_p - E_{p/2}$ = 43 mV is the same as the experimental value at low scan rates. Peak-widths in the 0.1 M $Ni^{II}(ClO_4)_2$ electrolyte were comparable with 0.1 M $Zn^{II}(ClO_4)_2$ and are shown in Figure S10.

On the basis of this analysis, the individual reduction and oxidation waves in 0.1 M $Ni^{II}(ClO_4)_2$ or 0.1 M $Zn^{II}(ClO_4)_2$ are found to be electrochemically quasi-reversible but chemically irreversible due to the structural change between $Ni^{II}(dtc)_2$ and octahedral $[Ni^{IV}(dtc)_3]^+$. The combination of these two chemically irreversible reactions produces an overall chemically reversible redox couple. This redox cycle is highly unique in the field of $2e^-$ electrochemistry and reminiscent of those observed for inorganic isomerization reactions for $1e^-$ transfer.[29,30] Such a large peak separation ($E_{pa} - E_{pc}$) is also typically associated with a wide peak-width ($E_p - E_{p/2}$) due to slow heterogeneous electron transfer kinetics. In the present case, the electron transfer and ligand transfer kinetics must be fast on the CV time scale in order to yield small peak-widths while the structural barrier is the main factor which determines the peak separation.

Redox Cycling Experiments. To test stability and efficiency of $[Ni^{IV}(dtc)_3]^+/Ni^{II}(dtc)_2$ as an effective catholyte in a nonaqueous RFB, chronopotentiometric cycling was performed using either $TBAPF_6$ or $Zn^{II}(ClO_4)_2$ as supporting electrolytes in an H-cell apparatus with carbon felt electrodes. Figure 10 shows the first complete cycle (i.e., oxidation followed by reduction) for 1 mM $Ni^{II}(dtc)_2$ in MeCN for a range of electrolyte conditions. Further cycles for each condition are shown in Figure S19. The anodic current

https://doi.org/10.1021/acs.inorgchem.2c03124
Inorg. Chem. 2022, 61, 19039−19048

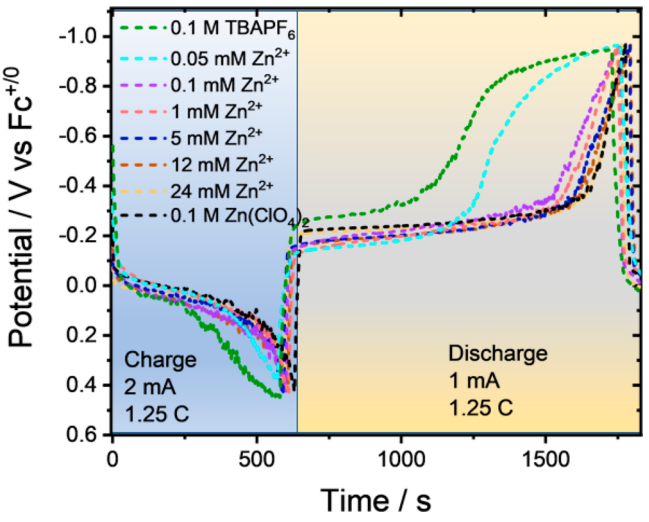

Figure 10. First complete cycles for chronopotentiometric oxidation of $Ni^{II}(dtc)_2$ followed by reduction of $[Ni^{IV}(dtc)_3]^+$ measured in a range of MeCN electrolyte solutions. As $Zn^{II}(ClO_4)_2$ was added to the solution, the potential curve for reduction of $[Ni^{IV}(dtc)_3]^+$ noticeably changed from two sequential $1e^-$ reductions to a single $2e^-$ reduction. Experiments were performed in an H-cell using an AMI-7000s membrane with 0.1 M $TBAPF_6$ in MeCN as the anolyte and 1 mM $Ni^{II}(dtc)_2$ in MeCN as the catholyte. The figure legend indicates the conditions for the background electrolyte in the catholyte chamber with $[Zn^{2+}]$ concentrations added to 0.1 M $TBAPF_6$ with the exception of 0.1 M $Zn(ClO_4)_2$ which contained no $TBAPF_6$.

(charging) was set to 2 mA (~6C rate) while the cathodic current (discharging) was set to 1 mA (~3C rate). The lower anodic current was found to be needed for complete discharge in the case of the 0.1 M TBAPF6 electrolyte. The individual $[Zn^{II}]$ values represent 0.1 M $TBAPF_6$ electrolytes with the indicated concentration of added $Zn^{II}(ClO_4)_2$.

In all cases, the oxidation process was largely unperturbed as a function of $[Zn^{II}]$ and showed a plateaued potential near 0 V vs $Fc^{+/0}$, indicative of $2e^-$ oxidation from $Ni^{II}(dtc)_2$ to $[Ni^{IV}(dtc)_3]^+$. This potential is more negative than what was observed for planar, glassy carbon electrodes. We believe this may be due to incomplete *iR* compensation or the high surface area and porous nature of the carbon felt electrode aiding second-order reactions such as ligand transfer and disproportionation of Ni^{III} intermediates by concentrating molecules in smaller volumes. The blue box indicates the expected time required to completely oxidize $Ni^{II}(dtc)_2$ to $[Ni^{IV}(dtc)_3]^+$ according to eq 1 with an applied current of 2 mA.

When the current was reversed, the reduction cycle showed two distinct plateaus in the case of 0.1 M $TBAPF_6$ with no added Zn^{II}. These potentials are consistent with sequential $1e^-$ reduction from $[Ni^{IV}(dtc)_3]^+ \rightarrow Ni^{III}(dtc)_3 \rightarrow [Ni^{II}(dtc)_3]^-$. Also note that the yellow box represents the expected time required to fully reduce $[Ni^{IV}(dtc)_3]^+$ back to $Ni^{II}(dtc)_2$ with a 1 mA applied current. The transition from one plateau to the next occurs at roughly the halfway point, indicating $1e^-$ reactions for each plateau. With only 0.1 mM $[Zn^{II}]$ added to the electrolyte (i.e., 10% of $[Ni^{II}(dtc)_2]$), the potential profile shifted to show only a single plateau at the first reduction wave near −0.2 V, which was maintained for almost the entire period of time expected for a $2e^-$ reduction. Increasing $[Zn^{II}]$ resulted in small increases in the total anodic and cathodic charges per cycle. At the best condition of 0.1 M $Zn^{II}(ClO_4)_2$, the difference in charging and discharging potentials was 0.25 V.

Extended battery cycling experiments were performed for the 0.1 M $Zn^{II}(ClO_4)_2$ and 0.1 M $TBAPF_6$ conditions to test the long-term stability of the Ni(IV/II) redox couple (Figure S20). These experiments were also performed with methyl viologen added to the anolyte chamber of the H-cell to provide a steady source of reversible redox active molecules to balance the current in the cell. In the cycling experiments reported above, no redox active molecule was added to the anolyte and thus redox chemistry of the MeCN solvent was expected to balance the current. This strategy works well for short time experiments but can lead to poor battery performance over longer periods of cycling time.

Figure 11a shows a comparison of the cathodic and anodic charges measured with chronopotentiometry for 1 mM

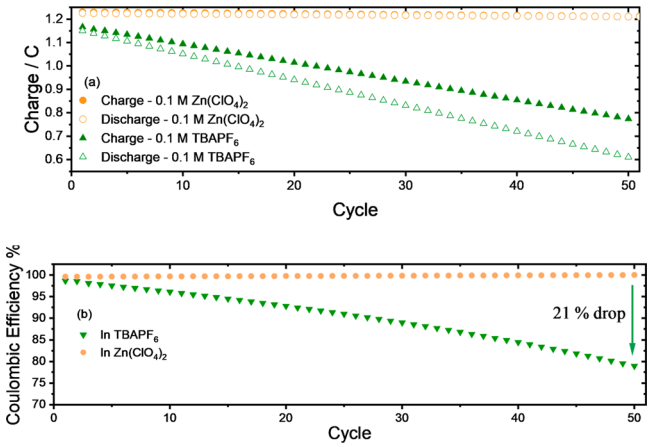

Figure 11. (a) Anodic and cathodic charges measured for each cycle during chronopotentiometry of 1 mM $Ni^{II}(dtc)_2$ in MeCN with either 0.1 M $Zn^{II}(ClO_4)_2$ or 0.1 M $TBAPF_6$ in the catholyte chamber. Maximum capacity = 1.25 C. (b) Coulombic efficiency comparison versus cycle number for $Zn^{II}(ClO_4)_2$ and $TBAPF_6$ electrolytes. All experiments were performed in an H-cell apparatus with an AMI-7000s membrane, 0.2 M $[MV](PF_6)_2$ with 0.1 M $TBAPF_6$ in MeCN as the anolyte, anodic current = 2 mA, and cathodic current = 1 mA.

$Ni^{II}(dtc)_2$ (1.25 C maximum capacity) for the two electrolyte conditions. In $Zn^{II}(ClO_4)_2$ electrolyte, both anodic and cathodic charges were initially 1.23 and 1.22 C, respectively, and only decreased by 2% for the duration of the 25 h cycle time. This indicates great stability of the Ni(IV/II) redox couple, despite the large structural reorganization and ligand transfer reactions that occur. In the $TBAPF_6$ electrolyte, the initial anodic and cathodic charges were found to be 1.17 and 1.16 C, respectively, but these values decreased as the cycle number increased, indicating degradation of the redox active molecules over time.

Taking the ratio of cathodic to anodic charge yields the Coulombic efficiency for each charge−discharge cycle which can give a measure of the molecular stability for each cycle. A comparison of this data for the two electrolytes is shown in Figure 11b. In the case of the $Zn^{II}(ClO_4)_2$ electrolyte, we observed ~97% columbic efficiency even after 50 cycles. In comparison to the $TBAPF_6$ supporting electrolyte, the Coulombic efficiency drops from an initial value of 96% to a final value of 75%, a 21% loss over the 25 h cycling time. This extreme loss in Coulombic efficiency is a clear indication that degradation of the redox active molecules is due to incomplete

https://doi.org/10.1021/acs.inorgchem.2c03124
Inorg. Chem. 2022, 61, 19039−19048

reduction during the sequential 1e$^-$ steps. The ability to reduce $[Ni^{IV}(dtc)_3]^+$ by 2e$^-$ at a single potential, thus produces a more stable battery over an extended period of time.

While these studies are not true redox flow experiments due to the H-cell configuration, they serve as proof-of-principle for the long-term stability of a 2e$^-$ LCET redox couple over continuous charge−discharge cycles. The use of Zn^{II} to increase the reversibility of 2e$^-$ transfer is a highly promising result that points to the ability to use $Ni^{II}(dtc)_2$ more effectively in these devices. Conventionally, substitutionally inert coordination compounds have been studied in RFBs to avoid degradation through ligand loss pathways.[10,13,31−33] While this can certainly be true, the studies presented here show that changes in the coordination environment can be used to our advantage to increase the number of electrons stored while maintaining a consistent potential upon charging or discharging. Provided that ligand transfer steps (or any chemical step of an ECE mechanism) are sufficiently fast such that conversion to the final 2e$^-$ oxidized or reduced states is faster than any degradation reactions then the molecular components should remain stable through multiple charge−discharge cycles.

In terms of applying the $[Ni^{IV}(dtc)_3]^+/Ni^{II}(dtc)_2$ redox cycle in functional RFBs, there are a number of advantages. The molecules store multiple electrons at an earth-abundant metal center, charge and discharge at consistent potentials, are cheap and easy to produce at large scales, and possess relatively low molecular weights. However, the redox cycle also has challenges which need to be addressed. Importantly, the number of electrons transferred per $Ni^{II}(dtc)_2$ is 4/3 (not 2) due to the sacrificial role of $Ni^{II}(dtc)_2$ in supplying dtc$^-$ ligands for the formation of $[Ni^{IV}(dtc)_3]^+$. Addition of the excess dtc$^-$ ligand was unsuccessful in this regard due to oxidation of the free ligand.[24] Therefore, there are inefficiencies in the maximum charge storage capacity. Additionally, solubility is quite low for these molecules in MeCN with 5 mM for $Ni^{II}(dtc)_2$ and 50 mM for $[Ni^{IV}(dtc)_3]BF_4$. Exchange of the ethyl groups on the dtc$^-$ ligand for *n*-butyl groups boosts the solubility for $Ni^{II}(dtc)_2$ to 35 mM; however, synthesis of new dithiocarbamate ligands with higher solubilities for the metal complexes will be required to fully utilize this class of molecules in RFBs. Research in the directions of increasing the charge storage density per molecule and molecular solubilities are currently being pursued by our group.

CONCLUSION

Examples of reversible 2e$^-$ transfer at monometallic coordination compounds are rare. The Zn^{II} catalyzed 2e$^-$ redox cycle of $[Ni^{IV}(dtc)_3]^+/Ni^{II}(dtc)_2$ reported here represents a unique example of this class of compounds that uses rapid intermolecular ligand transfer to facilitate multielectron LCET chemistry. Reductive Zn^{II} catalysis of $[Ni^{IV}(dtc)_3]^+$ to $Ni^{II}(dtc)_2$ is believed to be rooted in the chemical step of an ECE mechanism where Zn^{II} removes a dtc$^-$ ligand from $Ni^{III}(dtc)_3$ to form $[Ni^{III}(dtc)_2]^+$. On the oxidation side, we present evidence for an interaction between Zn^{II} and $Ni^{II}(dtc)_2$ that shifts the anodic peak for 2e$^-$ oxidation in the negative direction by 100 mV. The overall peak separation between 2e$^-$ oxidation and reduction is large due to the significant structural change from square planar $Ni^{II}(dtc)_2$ to octahedral $[Ni^{IV}(dtc)_3]^+$. Long-term battery cycling experiments show the essential nature of Zn^{II} catalysis in preserving the integrity of the redox active molecules, showing 97% Coulombic efficiency and 98% charge storage efficiency maintained for 50 cycles over 25 h. The high degree of reversibility and extending cycling experiments show that 2e$^-$ LCET redox couples could serve as effective redox active electrolytes in redox flow batteries.

ASSOCIATED CONTENT

Supporting Information

The Supporting Information is available free of charge at https://pubs.acs.org/doi/10.1021/acs.inorgchem.2c03124.

X-ray crystal structures, ESI-MS, cyclic voltammetry, ^{1}H NMR, rotating disk electrochemistry, diffusion coefficients, and chronopotentiograms (PDF)

Accession Codes

CCDC 2191919 and 2193154 contain the supplementary crystallographic data for this paper. These data can be obtained free of charge via www.ccdc.cam.ac.uk/data_request/cif, or by emailing data_request@ccdc.cam.ac.uk, or by contacting The Cambridge Crystallographic Data Centre, 12 Union Road, Cambridge CB2 1EZ, UK; fax: +44 1223 336033.

AUTHOR INFORMATION

Corresponding Author

Byron H. Farnum − *Department of Chemistry and Biochemistry, Auburn University, Auburn, Alabama 36849, United States;* orcid.org/0000-0001-9152-1909; Email: farnum@auburn.edu

Authors

Md. Motiur R. Mazumder − *Department of Chemistry and Biochemistry, Auburn University, Auburn, Alabama 36849, United States*

Niharika Dalpati − *Department of Chemistry and Biochemistry, Auburn University, Auburn, Alabama 36849, United States*

P. Raj Pokkuluri − *Department of Chemistry and Biochemistry, Auburn University, Auburn, Alabama 36849, United States*

Complete contact information is available at: https://pubs.acs.org/10.1021/acs.inorgchem.2c03124

Notes

The authors declare no competing financial interest.

ACKNOWLEDGMENTS

M.M.R.M., N.D., and B.H.F. acknowledge support from the National Science Foundation through a CAREER award CHE-1945160. This work appeared prior to publication as a preprint on ChemRxiv.[34]

REFERENCES

(1) Wang, W.; Luo, Q.; Li, B.; Wei, X.; Li, L.; Yang, Z. Recent Progress in Redox Flow Battery Research and Development. *Adv. Funct. Mater.* **2013**, *23* (8), 970−986.

(2) Yang, Z.; Zhang, J.; Kintner-Meyer, M. C. W.; Lu, X.; Choi, D.; Lemmon, J. P.; Liu, J. Electrochemical Energy Storage for Green Grid. *Chem. Rev.* **2011**, *111* (5), 3577−3613.

(3) Gong, K.; Fang, Q.; Gu, S.; Li, S. F. Y.; Yan, Y. Nonaqueous Redox-Flow Batteries: Organic Solvents, Supporting Electrolytes, and Redox Pairs. *Energy Environ. Sci.* **2015**, *8* (12), 3515−3530.

(4) Burgess, M.; Moore, J. S.; Rodríguez-López, J. Redox Active Polymers as Soluble Nanomaterials for Energy Storage. *Acc. Chem. Res.* **2016**, *49* (11), 2649−2657.

(5) Kamat, P. V.; Schanze, K. S.; Buriak, J. M. Redox Flow Batteries. *ACS Energy Lett.* **2017**, *2* (6), 1368−1369.
(6) Zhang, J.; Corman, R. E.; Schuh, J. K.; Ewoldt, R. H.; Shkrob, I. A.; Zhang, L. Solution Properties and Practical Limits of Concentrated Electrolytes for Nonaqueous Redox Flow Batteries. *J. Phys. Chem. C* **2018**, *122* (15), 8159−8172.
(7) Soloveichik, G. L. Flow Batteries: Current Status and Trends. *Chem. Rev.* **2015**, *115* (20), 11533−11558.
(8) Laramie, S. M.; Milshtein, J. D.; Breault, T. M.; Brushett, F. R.; Thompson, L. T. Performance and Cost Characteristics of Multi-Electron Transfer, Common Ion Exchange Non-Aqueous Redox Flow Batteries. *J. Power Sources* **2016**, *327*, 681−692.
(9) Sevov, C. S.; Hickey, D. P.; Cook, M. E.; Robinson, S. G.; Barnett, S.; Minteer, S. D.; Sigman, M. S.; Sanford, M. S. Physical Organic Approach to Persistent, Cyclable, Low-Potential Electrolytes for Flow Battery Applications. *J. Am. Chem. Soc.* **2017**, *139* (8), 2924−2927.
(10) Suttil, J. A.; Kucharyson, J. F.; Escalante-Garcia, I. L.; Cabrera, P. J.; James, B. R.; Savinell, R. F.; Sanford, M. S.; Thompson, L. T. Metal Acetylacetonate Complexes for High Energy Density Non-Aqueous Redox Flow Batteries. *J. Mater. Chem. A* **2015**, *3* (15), 7929−7938.
(11) Liu, Q.; Shinkle, A. A.; Li, Y.; Monroe, C. W.; Thompson, L. T.; Sleightholme, A. E. S. Non-Aqueous Chromium Acetylacetonate Electrolyte for Redox Flow Batteries. *Electrochem. Commun.* **2010**, *12* (11), 1634−1637.
(12) Huskinson, B.; Marshak, M. P.; Suh, C.; Er, S.; Gerhardt, M. R.; Galvin, C. J.; Chen, X.; Aspuru-Guzik, A.; Gordon, R. G.; Aziz, M. J. A Metal-Free Organic−Inorganic Aqueous Flow Battery. *Nature* **2014**, *505* (7482), 195−198.
(13) VanGelder, L. E.; Kosswattaarachchi, A. M.; Forrestel, P. L.; Cook, T. R.; Matson, E. M. Polyoxovanadate-Alkoxide Clusters as Multi-Electron Charge Carriers for Symmetric Non-Aqueous Redox Flow Batteries. *Chem. Sci.* **2018**, *9* (6), 1692−1699.
(14) Pierce, D. T.; Geiger, W. E. Structural Consequences of Electron-Transfer Reactions. Part XX. Splitting of a Two-Electron Cyclic Voltammetric Wave into Its One-Electron Components: The (.Eta.-C6Me6)2Ru2+/+/0) Couples. *J. Am. Chem. Soc.* **1989**, *111* (19), 7636−7638.
(15) Waldie, K. M.; Ramakrishnan, S.; Kim, S.-K.; Maclaren, J. K.; Chidsey, C. E. D.; Waymouth, R. M. Multielectron Transfer at Cobalt: Influence of the Phenylazopyridine Ligand. *J. Am. Chem. Soc.* **2017**, *139* (12), 4540−4550.
(16) Jude, H.; Krause Bauer, J. A.; Connick, W. B. An Outer-Sphere Two-Electron Platinum Reagent. *J. Am. Chem. Soc.* **2003**, *125* (12), 3446−3447.
(17) Mun, J.; Lee, M.-J.; Park, J.-W.; Oh, D.-J.; Lee, D.-Y.; Doo, S.-G. Non-Aqueous Redox Flow Batteries with Nickel and Iron Tris(2,2′-Bipyridine) Complex Electrolyte. *Electrochem. Solid-State Lett.* **2012**, *15* (6), A80.
(18) Savéant, J. M.; Costentin, C.*Elements of Molecular and Biomolecular Electrochemistry: An Electrochemical Approach to Electron Transfer Chemistry*, 2nd ed.; Wiley: Hoboken, NJ, 2019.
(19) Evans, D. H. One-Electron and Two-Electron Transfers in Electrochemistry and Homogeneous Solution Reactions. *Chem. Rev.* **2008**, *108* (7), 2113−2144.
(20) Bard, A. J.; Faulkner, L. R.*Electrochemical Methods: Fundamentals and Applications*; Wiley, 2000.
(21) Lachenal, D. Electrochemical Behaviour of Nickel (II) and Ni (IV) N,N-Diethyldithiocarbamates. Synthesis of a Nickel(IV) Species. *Inorganic and Nuclear Chemistry Letters* **1975**, *11* (2), 101−106.
(22) Hendrickson, A. R.; Martin, R. L.; Rohde, N. M. Dithiocarbamates of Nickel in the Formal Oxidation States I-IV. Electrochemical Study. *Inorg. Chem.* **1975**, *14* (12), 2980−2985.
(23) Mazumder, Md. M. R.; Burton, A.; Richburg, C. S.; Saha, S.; Cronin, B.; Duin, E.; Farnum, B. H. Controlling One-Electron vs Two-Electron Pathways in the Multi-Electron Redox Cycle of Nickel Diethyldithiocarbamate. *Inorg. Chem.* **2021**, *60* (17), 13388−13399.
(24) Richburg, C. S.; Farnum, B. H. Influence of Pyridine on the Multielectron Redox Cycle of Nickel Diethyldithiocarbamate. *Inorg. Chem.* **2019**, *58* (22), 15371−15384.
(25) Andrieux, C. P.; Grzeszczuk, M.; Savéant, J.-M. Electrochemical Generation and Detection of Transient Intermediates: Dimerizing Species. *Journal of Electroanalytical Chemistry and Interfacial Electrochemistry* **1991**, *318* (1), 369−372.
(26) Tonholo, J.; Boodts, J. F. C.; Goulart, M. O. F.; Sant'ana, A. E. G. The Electrochemical Behaviour, on Mercury, of Gossypol in the Acid PH Region in Mixed Aquo-Acetone Solvent. *J. Electroanal. Chem.* **1992**, *341* (1), 61−75.
(27) Sheldrick, G. M. A Short History of SHELX. *Acta Cryst. A* **2008**, *64* (1), 112−122.
(28) Bonamico, M.; Dessy, G.; Mariani, C.; Vaciago, A.; Zambonelli, L. Structural Studies of Metal Dithiocarbamates. I. The Crystal and Molecular Structure of the a Form of Nickel Diethyldithiocarbamate. *Acta Crystallogr.* **1965**, *19*, 619.
(29) Bond, A. M. Cyclic Fundamental and Second Harmonic a.c. Voltammetry with Phase-Selective Detection. *Journal of Electroanalytical Chemistry and Interfacial Electrochemistry* **1974**, *50* (2), 285−291.
(30) Wimmer, F. L.; Snow, M. R.; Bond, A. M. Electrochemical Investigations of Isomerism in Manganese and Group (VI) Dicarbonyl-Bis [1,2-Bis(Diphenylphosphino)Ethane] Complexes. *Inorg. Chem.* **1974**, *13* (7), 1617−1623.
(31) Sevov, C. S.; Fisher, S. L.; Thompson, L. T.; Sanford, M. S. Mechanism-Based Development of a Low-Potential, Soluble, and Cyclable Multielectron Anolyte for Nonaqueous Redox Flow Batteries. *J. Am. Chem. Soc.* **2016**, *138* (47), 15378−15384.
(32) Stauber, J. M.; Zhang, S.; Gvozdik, N.; Jiang, Y.; Avena, L.; Stevenson, K. J.; Cummins, C. C. Cobalt and Vanadium Trimetaphosphate Polyanions: Synthesis, Characterization, and Electrochemical Evaluation for Non-Aqueous Redox-Flow Battery Applications. *J. Am. Chem. Soc.* **2018**, *140* (2), 538−541.
(33) Sleightholme, A. E. S.; Shinkle, A. A.; Liu, Q.; Li, Y.; Monroe, C. W.; Thompson, L. T. Non-Aqueous Manganese Acetylacetonate Electrolyte for Redox Flow Batteries. *J. Power Sources* **2011**, *196* (13), 5742−5745.
(34) Mazumder, M. M. R.; Dalpati, N.; Pokkuluri, P. R.; Farnum, B. H. A Zinc Catalyzed Two-Electron Nickel(IV/II) Redox Couple: New Catholyte Design for Redox Flow Batteries. *ChemRxiv* **2022**, DOI: 10.26434/chemrxiv-2022-0b38t.